Supplementary Information for

Near-field Probing of the Local Density of Optical States Enhanced by Bound States in the Continuum in Nonlocal Metasurfaces

Jie Ji[1*], José A. Sánchez Gil[2], Djero Peeters[3], Wouter Holman[1], Thanh Xuan Hoang[4], Dook van Mechelen[3], Jaime Gómez Rivas[1*]

[1]Department of Applied Physics and Science Education, Institute for Complex Molecular Systems, and Eindhoven Hendrik Casimir Institute, Eindhoven University of Technology, Eindhoven, 5600 MB, Netherlands

[2]Instituto de Estructura de la Materia Consejo Superior de Investigaciones Científicas, Madrid, 20680, Spain

[3]Department of Electrical Engineering, Eindhoven University of Technology, Eindhoven 5600 MB, Netherlands

[4]Institute of High Performance Computing (IHPC), Agency for Science, Technology and Research (A*STAR), Singapore, 138632, Republic of Singapore

[*]E-mail:j.ji@tue.nl, j.gomez.rivas@tue.nl.

Contents

S1 Incidence angle-dependent measurements

Symmetry-protected BICs are manifested through the disappearance of diffraction bands, which result from the decoupling between plane waves and the periodic structure. Figure S1(a) shows the transmission spectra of the metasurface as a function of the angle of incidence. At normal incidence, no visible mode appears between 0.3 and 0.45 THz; the transmission is dominated by the "bright" mode at 0.5 THz, originating from the in-phase $\lambda/2$ resonance in the rods. Under oblique incidence, however, a leaky resonance emerges at lower frequencies. Off-normal excitation breaks the inversion symmetry of the system, causing the BIC to evolve into a quasi-BIC that becomes accessible from the far-field. As the angle increases, the quasi-BIC redshifts and broadens, reflecting a reduction in Q-factor.

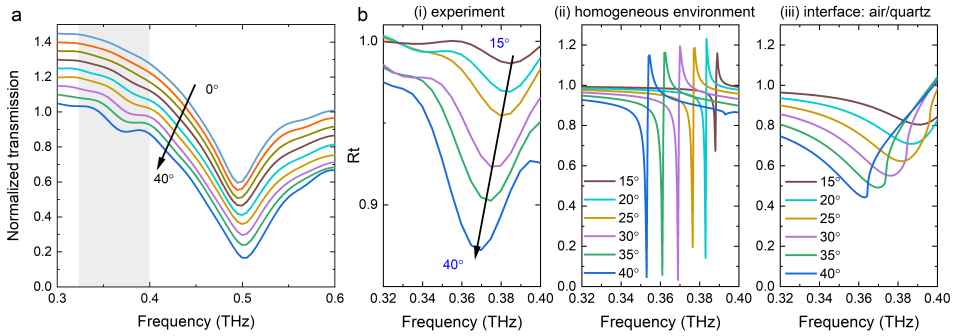

Figure S1: **Incidence angle-dependent transmission spectra of the metasurface.** (a) Normalized transmission spectra of the metasurface under different illumination angles, from $0°$ to $40°$ for y-polarized radiation. (b) Relative transmission spectra of the metasurface under oblique incidence normalized by the transmission under normal incidence: (i) experiment, (ii) Simulated relative transmission transmission on infinite size metasurface of perfect electric conductor (PEC) rods in an homogeneous environment, (iii) simulation of infinite metasurface of gold rods on a quartz substrate with realistic material losses.

These spectral changes are more pronounced in the relative transmission (Rt) spectra, where each oblique-incidence spectrum is normalized by the transmission at normal incidence to enhance the visibility of the quasi-BIC mode, as shown in Figure S1(b). The Rt spectra are

obtained from two simulation setups: one assuming gold rods embedded in a homogeneous dielectric, and another modeling the rods at the air–quartz interface with realistic material losses. The latter more closely replicates the experimental conditions.

The results clearly show that the quasi-BIC redshifts and its linewidth broadens with increasing incidence angles. The improved agreement between the second simulation and the experimental data confirms the critical roles of the dielectric interface and material absorption. Despite differences in dispersion behavior between the two simulation scenarios, both consistently reveal the emergence of a quasi-BIC mode near 0.395 THz. These findings highlight the BIC framework as an effective strategy for the design of nonlocal metasurfaces.

S2 THz near-field microscope

Figure S2 shows the THz near-field microscope with dual photoconductive microprobes. As shown in Figure S2(a), there are two three-dimensional (3D) motorized linear stages in this system for mounting the samples and the micro-probe for emission, respectively. In addition, the detector is mounted on a one-dimensional linear stage that moves along the z-axis. To ensure both probes are at the same height, we first use the method we refer to as "Approach-Touch-Release". In this approach, the sample is mounted on a three-dimensional motorized linear stage and is slowly and precisely moved toward the probes. As the sample approaches, contact is detected when the probe visibly touches the sample surface and bends, as observed through the optical camera shown in Figure S2(b). At the moment of contact, movement of the stage is immediately halted and then retracted in 1 μm steps until the probe returns to its original shape. This position is defined as the zero-height reference point (i.e., 0 μm above the sample surface). The same process is done for the emitter to confirm its height over the metasurface.

The distance between the two probes is precisely controlled using 3D motorized stages for mounting the emitter. The THz signal from the detector is recorded as the emitter is scanned

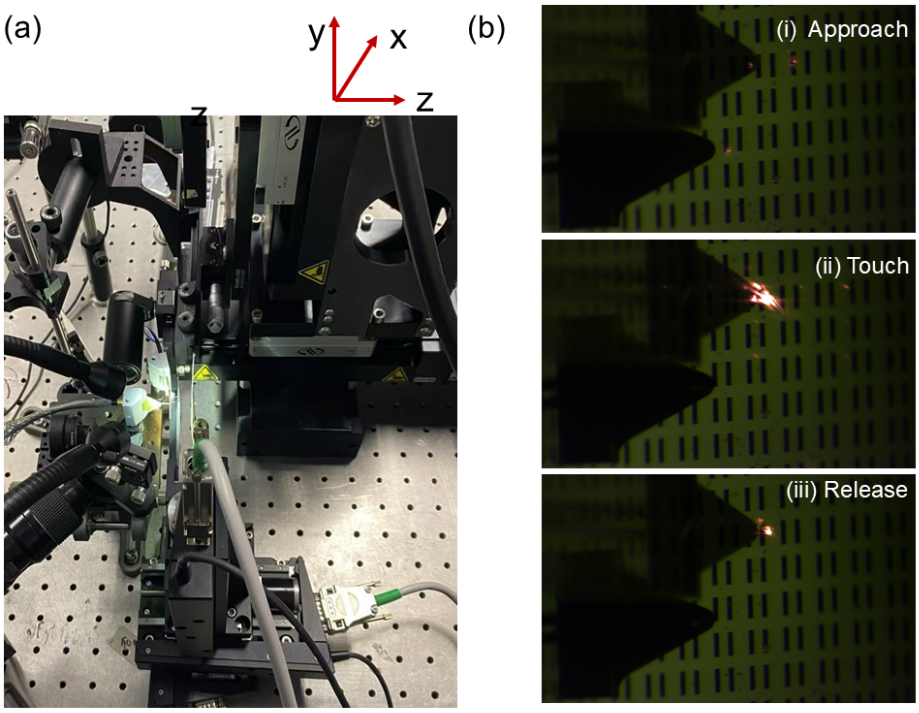

Figure S2: **The alignment of microprobes through 'Approach-Touch-Release'.** (a) Photo of the dual-photoconductive antenna based THz near-field microscope. (b) Camera view of the sample loading process: (i) Approach: moving the metasurface toward the microprobes with the precise three-dimensional linear stages; (ii) Touch: keep moving the metasurface until it touches probes, which can be observed through the camera; (iii) Release: When the metasurfaces touches the probes, stop the movement and move it backward 10 μm.

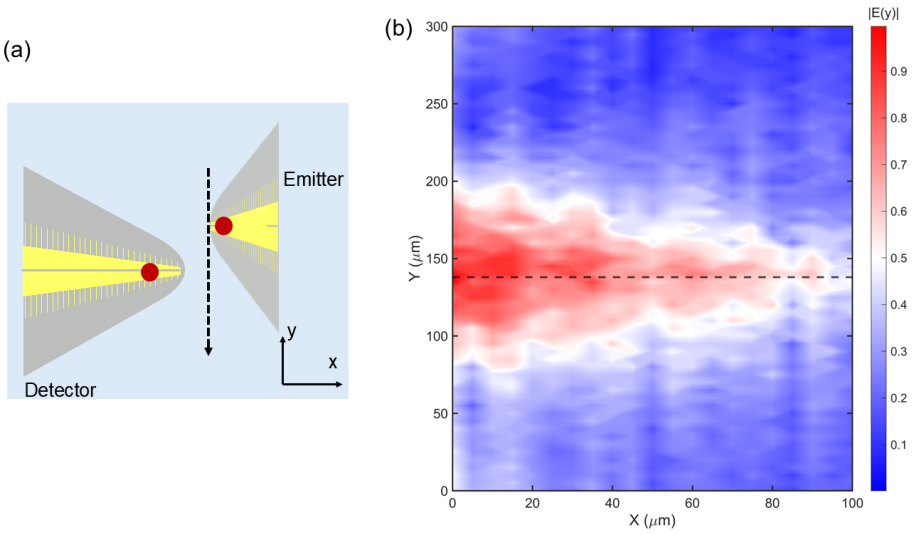

Figure S3: (a) Schematic illustration of the emitter movement over the xy plane to confirm the relative distance between the probes. (b) Spatial mapping of THz amplitude $|E(y)|$ at 0.3 THz measured by the detector when the micro-sized emitter is moving over xy plane, here '0' indicates the initial starting position for the emitter.

along the y-axis, from a position above to another position below the detector. This scanning allows us to identify the position of maximum signal intensity, which we define as the lateral center of the detector. To more accurately determine this central y-position, Figure S3 presents a spatial mapping of the emitter as it also moves over a 100 μm range along the x-axis. The results clearly show that, across all x-positions, the maximum signal consistently occurs at approximately 138 μm along the y-axis (with the starting position labeled as '0'). This confirms the central position of the detector along the y-direction.

Lastly, the emitter is moved along the x-axis toward the detector until physical contact is observed with the camera. At this point, the laser beam on the microprobes begins to shake, as shown in Figure S2 (ii), indicating the contact. This point is defined as the zero position along the x-axis. During the measurement, the emitter is retracted by 20 μm along the x-axis and 10 μm along y-axis to prevent the excitation laser from undergoing multiple reflections between the closely spaced microprobes.

S3 Spatial resolution of THz near-field microscope

The effective spatial resolution of our THz near-field microscope is approximately 20 μm, in line with the specifications of the photoconductive antennas (PCAs) and the overall optical configuration. This estimate is based on system geometry, the optical alignment of the dual probes, and the response characteristics of the PCAs. We employed the line spread function (LSF) method to validate the system resolution. The LSF, a commonly used concept in optics and imaging, characterizes how an optical system responds to a narrow, line-shaped input and serves as the one-dimensional analogue of the point spread function.

To validate the system's spatial resolution, particularly for probing the PLDOS of the gold rods in our sample, we fabricated a line array of metal strips with widths ranging from 5 μm to 35 μm, and a thickness of 100 nm, as shown in Figure S4. Each strip is 1 mm in length. A line scan was performed across the array using the THz near-field microscope with a step size of 5 μm and the probe at a height of 10 μm. The lateral separation between the two microprobes was 20 μm along the direction of the line scan (x) and 10 μm perpendicular to this direction (y). Figure S4(b) presents the measured THz intensity spectra at each scan position. This field enhancement remains clearly detectable even for the 5 μm-wide metal strips, highlighting the system's ability to detect subwavelength metal features, as shown in Figures S4(b) and (c). The linewidth of the intensity peak obtained by fitting the averaged THz intensity profile (integrated between 0.7 THz and 1.0 THz) with a Gaussian function in Figure S4(c), appears broader than the intrinsic spatial resolution of the microprobes. This broadening is primarily attributed to the 20 μm lateral separation between the two microprobes used during the measurement.

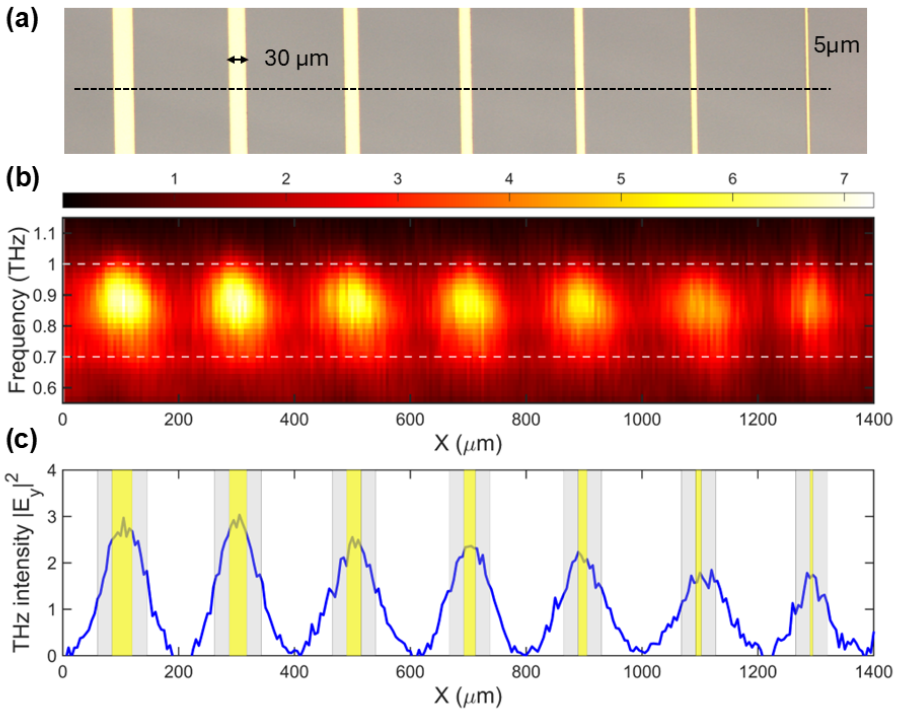

Figure S4: **Spatial resolution of the THz near-field microscope.** (a) Optical image of the metallic strips with different widths from 5 μm to 35 μm at a step of 5 μm. During the measurement, the microprobes are placed at a height of 10 μm over the sample surface. (b) 2D colorplot of the measured THz near-field intensity spectra with a line scanning over the of metal strips. (c) THz field intensity of the line scanning over the metal strips at 0.88 THz. The yellow marked region represents the metal strips.

S4 Effect of the titled angle of the emitter on the quasi-BIC mode

In our study, the quasi-BIC mode is excited by a near-field point dipole source (photoconductive antenna) placed in close proximity (approximately 10 μm) to the metasurface, as shown in Figure S5(a). Unlike plane-wave excitation, which is subject to well-defined incidence angles and symmetry constraints, a point dipole emitter inherently lacks translational symmetry and exhibits a broad angular spectrum. As a result, this localized source can couple to all the available modes, including those that are symmetry-protected from far-field radiation. Importantly, it leverages local symmetry breaking at the excitation site without altering the intrinsic radiation symmetry of the mode. Since the far-field radiation channel remains forbidden due to the global symmetry of the structure, the excited quasi-BIC mode continues to exhibit a high Q-factor, consistent with its bound nature.

Regarding the orientation of the emitter, although the near-field dipole is slightly tilted (as shown in Figure S5(b), this tilt does not significantly affect the E_y component of the emitted THz electric field, the component responsible for coupling to the BIC in the metasurface. Therefore, the tilt angle θ does not appreciably alter the coupling efficiency, resonance linewidth, or Q-factor of the BIC mode under this specific excitation geometry.

S5 Collective response of the BIC mode.

To illustrate that the BIC corresponds to the collective response of the dimer array, Figure S6 presents the calculated frequency-dependent enhancement of the PLDOS, $\mathrm{Im}(G_{yy})/\mathrm{Im}(G_0)$, along the y-direction from 0.3 to 0.45 THz. The PLDOS is evaluated at a point located halfway across the width of one rod in the central dimer, for arrays with increasing numbers of dimers $N \times N$. For a single dimer ($N = 1$), only one broad PLDOS peak is observed. As N increases,

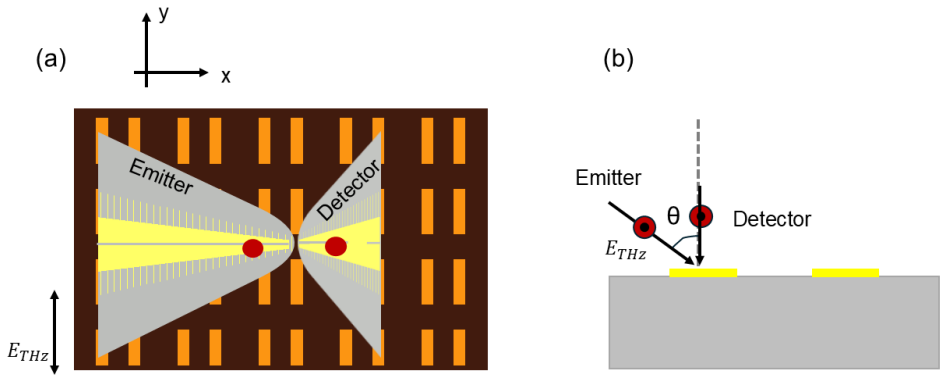

Figure S5: (a) Illustration of the THz near-field measurement on the metasurface. (b) Schematic representation of THz electric field direction of the emitter and detector corresponding to the orientation of the rods during the measurement.

sharp peaks emerge in the spectra and become progressively narrower, indicating increasing coherence and stronger modal confinement. Notably, the lowest-frequency peak blue-shifts with increasing array size and converges toward 0.395 THz. The corresponding field distributions in Figure S6(a)-(d) reveal that the mode extends into neighboring unit cells—evidence of the collective resonant behavior responsible for the formation of the BIC.

To further explore the collective response of the array to the formation of the BIC mode, Figure S7 (a) displays the spectrum of PLDOS enhancement $\mathrm{Im}(G_{yy})/\mathrm{Im}(G_0)$ for the metasurface with 9×9 dimers and the respective spatial distribution of the PLDOS enhancement at each resonant peak of the spectrum. There are seven peaks in the spectrum of the PLDOS enhancement. Peaks 4th and 6th are relatively weak and broad. Therefore, the PLDOS enhancement is not as significant compared to that observed for the sharper peaks, specifically the 1st, 2nd, 3rd, 5th, and 7th. These sharp peaks correspond to collective hybridized modes formed through the coherent coupling of localized resonances across the unit cell array. In finite structures, these modes manifest as standing-wave field patterns that span the entire array, resembling cavity-like behavior arising from interference and multiple scattering within the system. As the array size

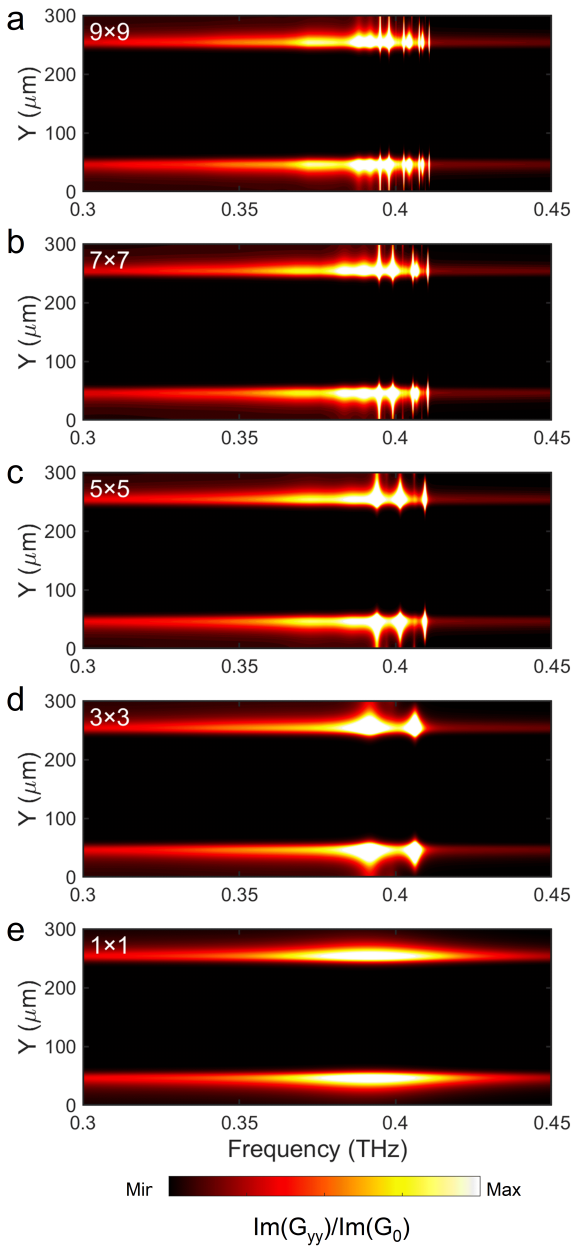

Figure S6: **PLDOS enhancement.** Calculated PLDOS enhancement as a function of frequency and position along the y-direction at half of the width of one rod of the central dimer in arrays with different numbers of dimers. (a) 9×9, (b) 7×7, (c) 5×5, (d) 3×3, and (d) 1×1.

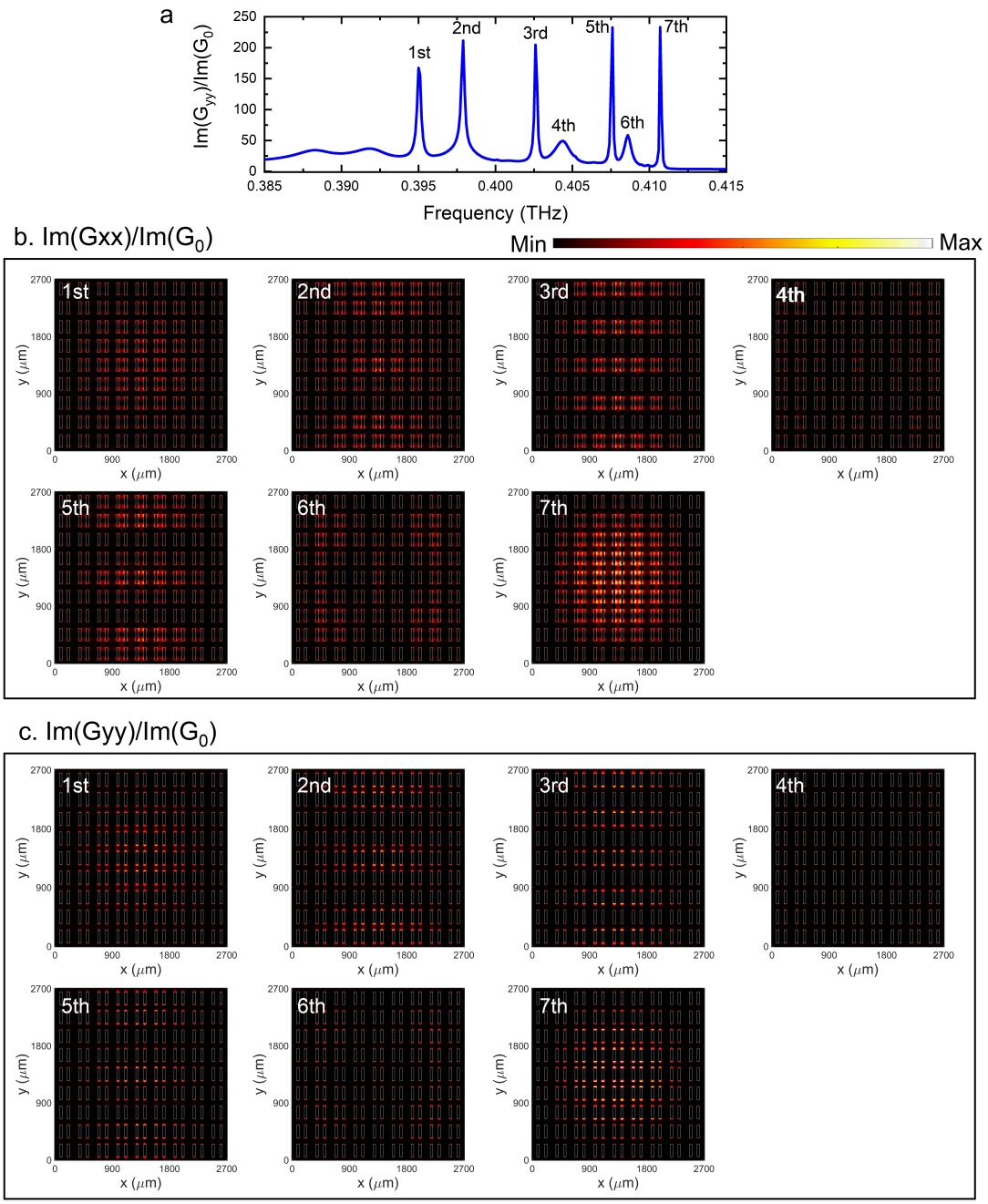

Figure S7: **Spatial distribution of the PLDOS enhancement.** (a) Spectrum of the calculated PLDOS enhancement for the 9 $\times$ 9 dimers metasurface. (b) Calculated spatial distribution of the PLDOS enhancement along the x-direction, $\mathrm{Im}(G_{xx})/\mathrm{Im}(G_0)$, at the frequencies of the different peaks in (a). (c) Calculated spatial distribution of the PLDOS enhancement along the y-direction, $\mathrm{Im}(G_{yy})/\mathrm{Im}(G_0)$, at the frequencies of the different peaks in (a).

increases, these peaks are expected to narrow further, eventually becoming vanishingly narrow modes that represent the BIC in a sufficiently large array.

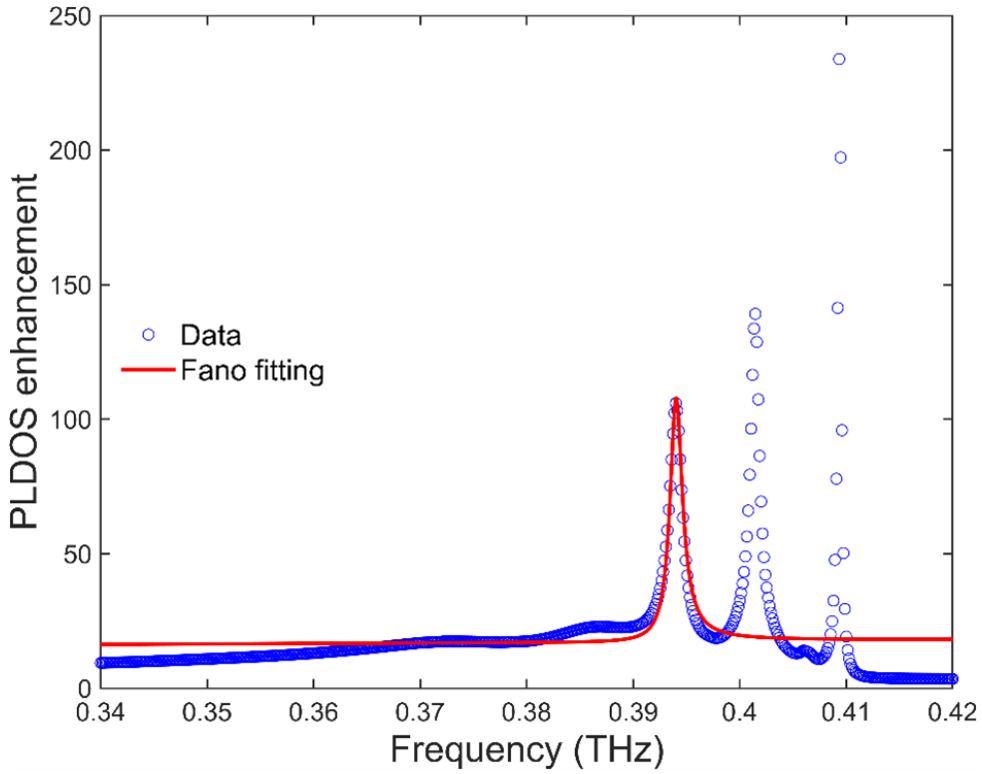

Figure S8: Simulated PDOS for the 5×5 array at the central unit cell. The red curve is a fit to the lowest frequency resonance using a Fano line profile. From the fit, the Q-factor is obtained.

As explained above, there are more than one peak in the PLDOS enhancement spectra, while the first one is identified as the fundamental mode of the BIC mode. Here, we take the metasurface with finite size $N = 5$ ($N \times N$ being the total number of unit cells) as an example to illustrate the procedure to obtain the Q-factor of such fundamental mode in Figure S8. The size-dependent Q-factor is extracted from the frequency-dependent PLDOS enhancement spectra by performing a Fano line-shape fitting on the first resonant peak using the following equation,

$$y(f) = A \cdot \frac{\left(q + \frac{2(f - f_0)}{\Delta f}\right)^2}{1 + \left(\frac{2(f - f_0)}{\Delta f}\right)^2} + B, \tag{1}$$

where f_0 is the peak frequency, Δf is full width at half maximum (FWHM), and q is Fano asymmetry parameter. In addition, A and B are scaling and offset constants, respectively. The quality factor is then calculated as $Q = f_0/\Delta f$. This method provides an accurate characterization of the fundamental resonance associated with the BIC mode.

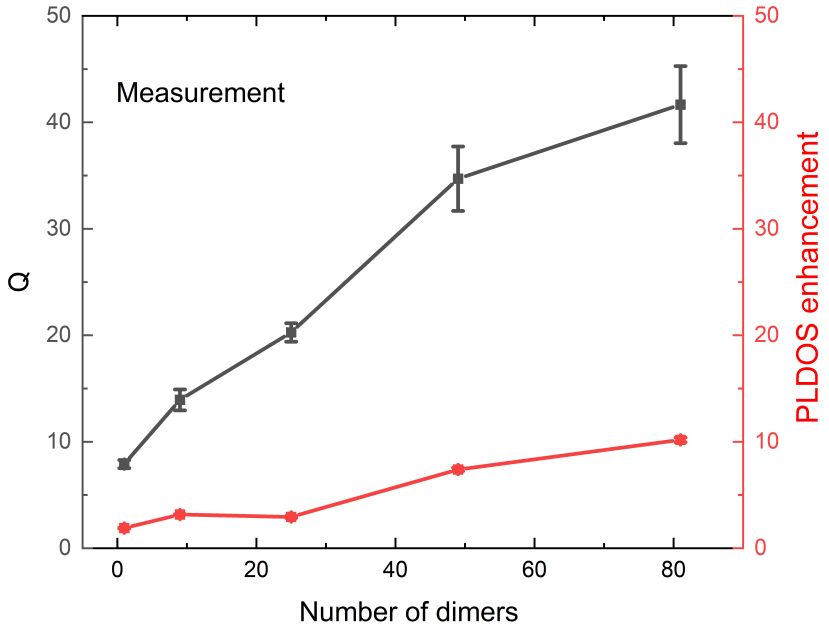

Figure S9: Measured Q-factor and PLDOS enhancement as a function of the total number of unit cells in finite metasurfaces.

Figure S9 presents the measured Q-factor and PLDOS enhancement as a function of the dimer array size in the finite metasurface. Both quantities initially increase with array size, reflecting the growing coherence and collective response of the system. The PLDOS enhance-

ment saturates as the metasurface becomes larger, in good agreement with simulation results. In contrast, the Q-factor appears to saturate at $N = 9$, deviating from the simulated trend. This discrepancy is primarily attributed to the limited frequency resolution (20 GHz) of our measurement system. Moreover, the experimentally measured values are systematically lower than those predicted by simulations, due to a combination of limited resolution, intrinsic material losses, and substrate effects not fully captured in the simulations.

S6 Near-field measurements of the phase

In Figure S10(a), we present the phase distribution corresponding to the PLDOS measurement shown in Figure 4(e) of the main text. For PLDOS measurements, the two probes are scanned together, since by definition, $\rho_0(r_0, \omega) = (2\omega n^2)/(\pi c_0^2) Tr[Im(G_0(r_0, r_0, \omega))]$, the emitter and detector must be placed at the same position r_0. As a result of this configuration, the two rods within each dimer appear nearly symmetric, and the characteristic π phase difference of the antisymmetric quasi-BIC mode is not directly visible in Figure S10(a). To resolve the phase relationship between the two bars of a dimer, we performed additional measurements with the emitter fixed at the edge of a rod under y-polarized excitation, while scanning the detector probe across the unit cell as shown in Figure S10(b–c). The measurements correspond to the cross density of optical states (CDOS), $\rho_{CDOS}(r, r_0, \omega) = (2\omega n^2)/(\pi c_0^2) Tr[Im(G_0(r, r_0, \omega))]$, where the emitter is fixed at position r_0 and the detector is placed at position r and mapped within the closed dashed box in S10(b-c), with a step size of 15 μm. In Figure S10(b), the detector was y-polarized; in Figure S10(c), the detector was z-polarized. In both measurements, the phase maps clearly show that the two rods within a dimer oscillate out of phase by π at the resonance frequency (0.395 THz). For the y-polarized detector, as shown in Figure S10(b), the probe is sensitive to the in-plane electric field aligned with the excitation polarization. In this case, the detected phase directly reflects the opposite charge oscillations on the two rods: when one

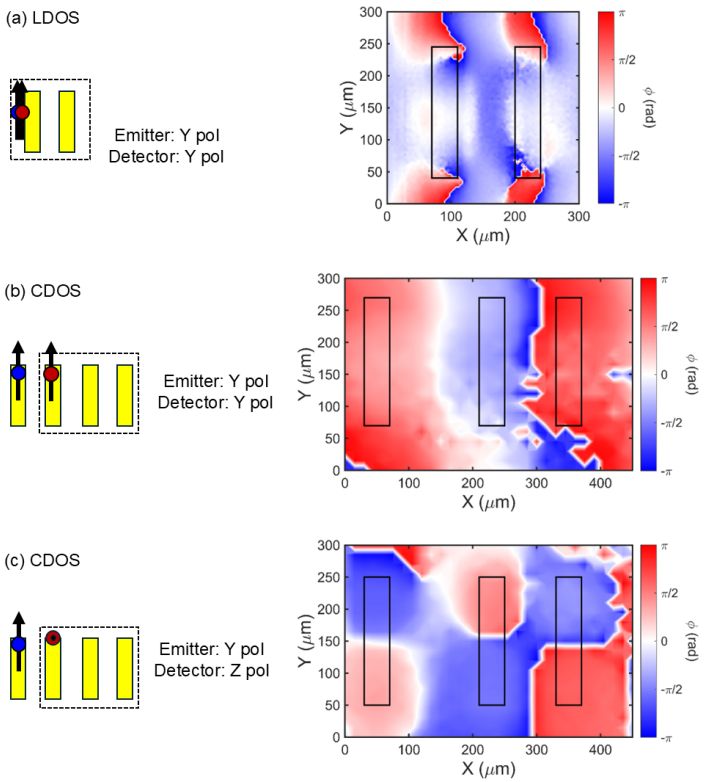

Figure S10: **Phase-resolved near-field maps of the dimer metasurface at the BIC resonance.** (a) Phase distribution corresponding to the PLDOS measurement over one unit cell, obtained with a y-polarized point emitter and detector scanned together at fixed relative position. (b) Phase distribution over one and a half unit cells, measured with the y-polarized emitter fixed at the edge of one rod and the y-polarized point detector scanned within the dashed box with 15 μm steps in both x and y directions. (c) Phase map under the same excitation, but with the z-polarized point detector scanned within the dashed box with 15 μm steps in both x and y directions.

rod carries a positive charge at its tip, the other carries a negative charge, yielding an overall π phase shift across the dimer. For the z-polarized detector, as shown in Figure S10(c), the probe measures the out-of-plane component of the near field, which arises from the discontinuity of the in-plane current distribution at the rod edges. Because the in-plane currents in the two rods are antiparallel, the corresponding out-of-plane fields also exhibit a π phase difference.

S7 Spatial distribution of the PLDOS enhancement under x-polarized excitation and detection

The PLDOS is measured when the emitter possesses a dipole moment oriented along a principal axis, and the adjacent detector is sensitive only to the corresponding polarization. Since the THz microprobes used in our setup are polarization-sensitive, the PLDOS along the x-direction can be measured by simply rotating the sample by $90°$. Figure S11 shows the spatial distribution of both the calculated $\mathrm{Im}(G_{xx})/\mathrm{Im}(G_0)$ and the experimentally measured $\mathrm{Im}(E_x(\mathbf{r_0},\omega))/\mathrm{Im}(E_0(\mathbf{r_0},\omega))$ under x-polarized local excitation and detection, at three different frequencies. When the emitter is placed at a height of $z = 10$ μm above the surface, the PLDOS reaches its maximum enhancement at the BIC frequency (0.395 THz).

In contrast to the PLDOS enhancement observed at the rod edges under y-polarized excitation, the x-polarized excitation leads to PLDOS maxima at the corners of each rod, as shown in Figure S11(b). As the detection point moves farther from the surface, the locations of peak PLDOS enhancement shift toward the center between the ends of the two rods, as seen from both the calculations in Figure S11(e) and measurements in Figure S11(h), respectively.

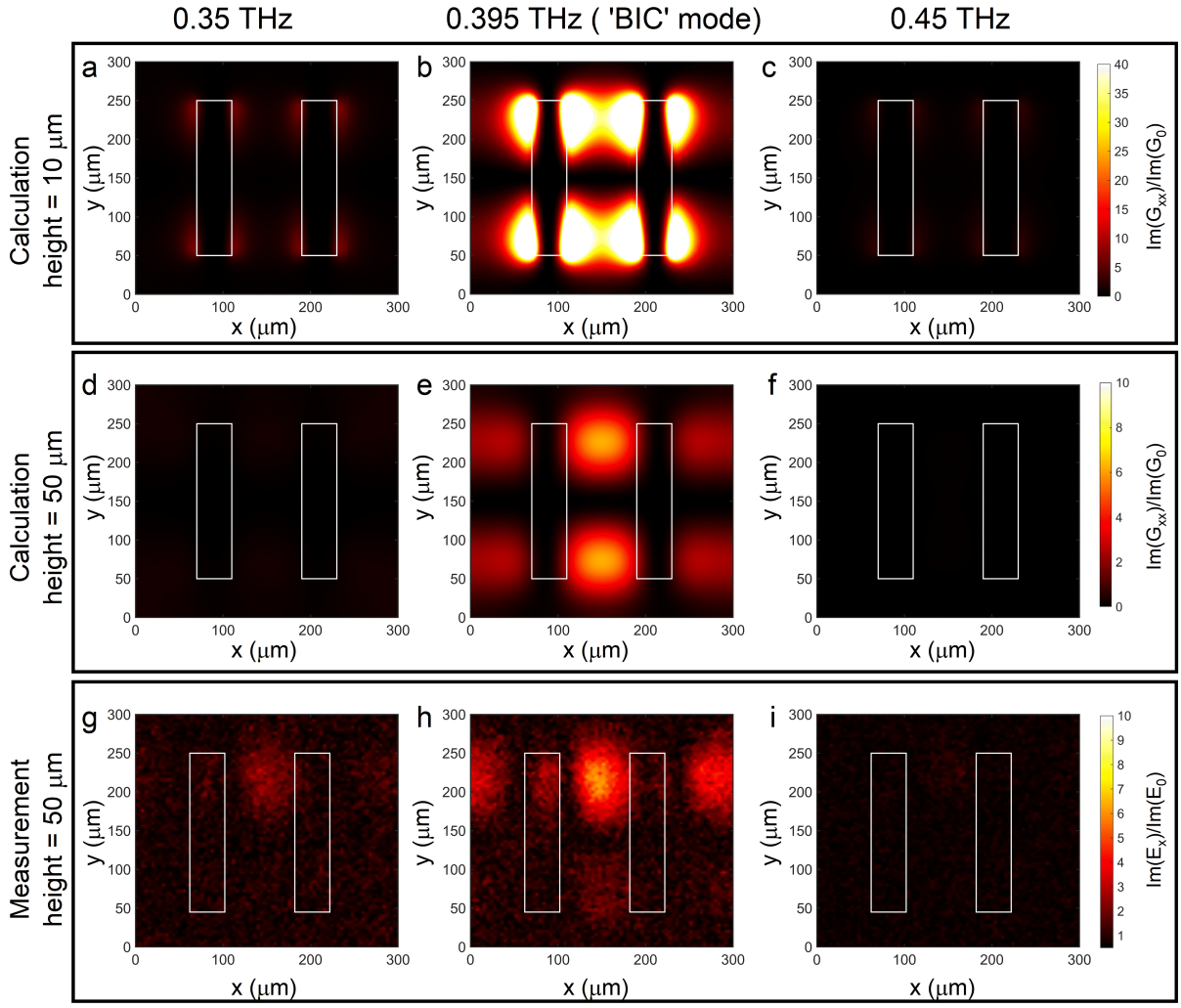

Figure S11: **Calculated spatial distribution of P_{xx}/P_0 over the central unit cell in a 9 $\times$ 9 dimer array at the frequencies of 0.35 THz, 0.395 THz, and 0.45 THz, and at different heights**. (a-c) Height of 10 μm, and (d-f) height of 50 μm. (g-i) Measured spatial distribution of P_{xx}/P_0 at a height of 50 μm over one unit cell of the metasurface at the frequencies of 0.35 THz, 0.395 THz, and 0.45 THz, respectively.

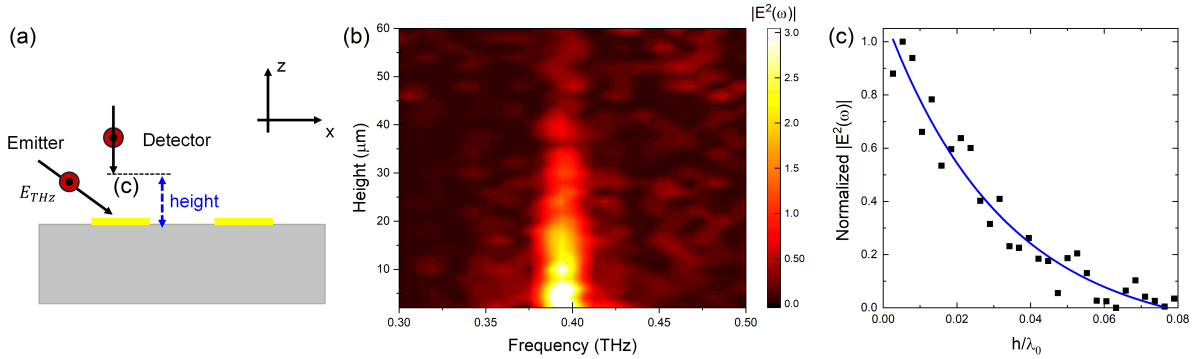

Figure S12: **Out-of-plane confinement of the quasi-BIC mode to the surface.** (a) Illustration of the measurement setup; (b) 2D colorplot of the measured THz field intensity as a function of frequency and height of the detection probe over the surface. (c) Normalized THz intensity as a function of height at the quasi-BIC. The symbols are the measured data, and the curve is the fitted result with an exponential decay function $y = y_0 + Aexp((h - h_0)/\tau)$.

S8 Out-of-plane confinement of the quasi-BIC mode to the surface

To further confirm that the resonance corresponds to a surface-confined mode rather than trivial attenuation of a point-source signal, we performed an additional height-dependent measurement in which the emitter remained fixed relative to the metasurface, while the detector probe was precisely translated away from the sample in 2-μm steps, as illustrated in Figure S12(a). At each height, we recorded the detected THz transient. The 2D map in Figure S12(b) shows a clear field enhancement at the quasi-BIC frequency (0.395 THz), which rapidly disappears within 25 μm above the surface. The extracted resonance amplitude versus height is plotted in Figure S12(c). The measured data (symbols) are well described by an exponential decay function, $y = y_0 + Aexp((h - h_0)/\tau)$, where τ is the decay length. The fitted decay constant corresponds to $\tau \approx 0.032\lambda_0$ ($\approx 20\mu$m for $\lambda_0 \approx 760$ μm). This sub-wavelength confinement length is consistent with the evanescent nature of a symmetry-protected quasi-BIC mode and is in excellent agreement with the rapid PLDOS decay observed in our main measurements.

By contrast, a simple reduction of point-source coupling with probe height would lead to a broadband attenuation rather than the sharp, frequency-selective exponential decay we observe. These results confirm that the disappearing resonance signal with increasing height is a direct signature of the spatial confinement of the quasi-BIC mode to the metasurface, and not a trivial consequence of weakened excitation.